

Real-time modeling of three-dimensional granular intrusion

Shashank Agarwal^a, Daniel I Goldman^b, and Ken Kamrin^a

^aDepartment of Mechanical Engineering, Massachusetts Institute of Technology, Cambridge; ^bDepartment of Physics, Georgia Institute of Technology, Atlanta

This manuscript was compiled on May 31, 2022

Granular intrusion is common in a range of processes including ballistic impact and penetration problems, and locomotion of humans, animals, and vehicles in natural terrains. The computational cost of full-scale numerical modeling is high, whereas a capability to model such scenarios in real-time is critical in applications such as path planning and efficient maneuvering of vehicles in sandy terrains and extraterrestrial environments. Existing reduced-order methods that model intrusion have limited capabilities due to their shape- and media-specific forms. This work formulates a reduced-order modeling technique, 3-dimensional Resistive Force Theory (3D-RFT), capable of accurately and quickly predicting the resistive force on arbitrary-shaped bodies moving in grains. Aided by a continuum mechanical description of the granular bed, a comprehensive set of symmetry constraints, and a large amount of reference data, we develop a self-consistent and accurate form for 3D-RFT. We verify the model capabilities in a wide range of cases and show it can be quickly recalibrated to different media and intruder surface types.

Granular intrusion | Resistive Force Theory | Continuum modeling | Reduced-order models

Granular intrusion is a common occurrence in the natural and human-made worlds, arising in biological and vehicular locomotion, excavation and anchoring applications, and meteorite and ballistic impact problems (1–4). Modeling intrusion in real-time is critical for a variety of applications and would enable heuristic understanding and quick insight into phenomena like biological circumnavigation (5) and robot-terrain interactions (6). But the multiphase nature of the granular media — simultaneous solid- and fluid-like behaviors (7) — makes modeling such systems computationally challenging. Despite over a century of progress in the disciplines of granular physics and *terramechanics* — the study of the interaction of tracked vehicles on various substrates (8) — challenges remain. Many commonly used methods have limited applicability due to their shape- or media-specific nature. For instance, commonly used terramechanical empirical models such as the Bekker model (9) (later modified by Wong and Reece (10)) and Magic formulae (11) are limited to specific geometries such as circular wheels. Inspired by an analogous approach for viscous fluids (12, 13), in recent years a granular Resistive Force Theory (RFT) has been introduced to model the forces on arbitrarily shaped intruders in granular media, but its form is limited to 2-dimensional problems. This poses limits on its usage in many practical applications.

In this work, we introduce a method for predicting the granular resistive forces on arbitrarily shaped three-dimensional bodies moving in arbitrary ways in a granular media. This work extends the work of 2-dimensional granular resistive force theory (2D-RFT) proposed by Li et al. (14) to 3-dimensions.

Attempts to extend RFT to 3D intruders have only recently been explored (5, 15). However, the previous approaches have limited robustness as the forms chosen lack a direct connection to granular mechanics, they do not always satisfy the needed self-consistency constraints from symmetry, and they were tested against non-exhaustive input and output data sets which masked certain incorrect force regimes (see Sec 1 of Supplemental Information). We overcome these limitations to propose a 3D-RFT framework that is easy to use and quick to recalibrate for a variety of granular media and surface roughnesses. The analysis is informed by a large data-set generated using a validated granular mechanics continuum model. We then examine predictions of the resulting 3D-RFT against a variety of granular intrusion tests, consisting of the arbitrary motion of many symmetric and asymmetric shapes in beds of granular media, and find an excellent agreement between the reference results and 3D-RFT predictions both globally (total intrusion force and moment) and locally (surface stress distribution).

1. Introduction

Generic RFT form. The Resistive Force Theory methodology was originally introduced by Gray and Hancock (12) for modeling self-propelling undulatory biological systems in viscous fluids. In this model, a simple approximate formula for the resistive force on a segment of a thin body is derived from the Stokes equations as a function of the segment’s velocity components, orientation, and a few variables characterizing the fluid-segment interaction. Importantly, the theory assumes decoupling of the forces over the various segments of the body (13). The success of fluid RFT motivated multiple studies (14, 16, 17) to explore the existence of a similar theory in granular media.

Li et al (14) proposed a planar (or 2-dimensional) version of RFT for dry granular media (2D-RFT). In 2D-RFT, at

Significance Statement

This work proposes a general theory for modeling diverse granular intrusion problems such as animal and human locomotion in sands and other natural terrains. Respecting numerous physical constraints, the theory allows for modeling arbitrary motion of three-dimensional generally-shaped objects in granular media in near real-time. This theory is a crucial step in developing robust, reliable, and fast methods for modeling granular interactions. The work also provides a blueprint for developing physics-informed reduced-order models for other media.

²To whom correspondence should be addressed. E-mail: kkamrin@mit.edu

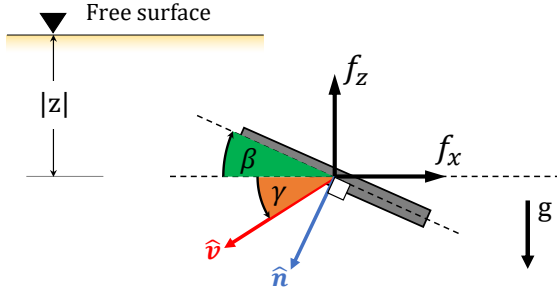


Fig. 1. 2D RFT sub-surface characterization: Any moving sub-surface is represented using a set of two characteristic angles — plate tilt (β , green) and angle of attack (γ , orange).

low-speeds, the rate-independent nature of granular media (characterized by low values of the non-dimensional (micro-) inertial number I (18–20) and macro-inertial number I_{mac} , see Materials and Methods) makes the dependence of intrusion force independent of the velocity magnitude. Assuming material strength increases with pressure and that pressure is primarily due to gravity, Li’s 2D-RFT model has the following form:

$$\mathbf{F}_{\text{total}} = \int_{\text{surf}} ((\alpha_x^{\text{mat}}(\beta, \gamma), \alpha_z^{\text{mat}}(\beta, \gamma)) |z| ds. \quad [1]$$

Here, $\mathbf{F}_{\text{total}}$ represents the total force on an intruding surface, which is divided into smaller planar sub-surface elements of area ds and depth $|z|$ from the free surface. The *tilt angle* β and *angle of attack* γ characterize the orientation and motion of each surface element of the intruding body (see Fig 1). The vector-valued function of angles $\boldsymbol{\alpha}^{\text{mat}} = (\alpha_x^{\text{mat}}, \alpha_z^{\text{mat}})$ represents the force per unit area per unit depth; this function must be obtained a priori through experiments or simulations of plate drag and depends on the material properties of the granular media, the intruder surface interaction, and the value of gravity. Of note, Eq 1 assumes no correlation between the forces on different sub-surfaces; only details local to a surface element determine the force on that element (16). A comprehensive comparison of various existing reduced order methods for modeling granular intrusions, including 2D-RFT and a *terramechanical* model, can be referred from Agarwal et al. (2).

In recent years, it has been shown that plasticity-based PDE models can also obtain the form of 2D granular RFT (21). More recently, the performance of the continuum approach in modeling a variety of granular intrusions has been demonstrated for wheeled locomotion, impact and penetration, and multi-body intrusion (2, 22–25). Additionally, the approach also provides insight into the somewhat surprising observation that granular RFT is often more accurate than its viscous fluid counterpart (12, 13). Thus, while experimental observations primarily drove the original RFT discoveries, the availability of faster computational methods, the success of 2D-RFT, and a need for better real-time 3D granular intrusion methods have driven the exploration of 3D-RFT. Our work combines the capabilities of the continuum approach with a few symmetry requirements and DEM data to accurately and efficiently model the physics of 3-dimensional granular intrusion to develop a 3D-RFT. We briefly discuss the details of the continuum approach next.

2. Continuum modeling

We use continuum modeling as the primary theoretical motivator as well as a reference data generation tool in this work. The constitutive model we use (22, 23) has a dense response characterized by a rate-insensitive, non-dilatant frictional flow rule, but also models the separated state which allows material to become stress-free when below a *critical density*. The model has been validated in a number of previous studies of granular intrusion and locomotion (21, 25–28).

The constitutive flow equations representing the material’s separation behavior, shear yield condition, and tensorial co-directionality, respectively, are shown below:

$$\begin{aligned} (\rho - \rho_c)P &= 0 \quad \text{and} \quad P \geq 0 \quad \text{and} \quad \rho \leq \rho_c, \\ \dot{\gamma}(\tau - \mu_{\text{int}}P) &= 0 \quad \text{and} \quad \dot{\gamma} \geq 0 \quad \text{and} \quad \tau \leq \mu_{\text{int}}P, \\ D_{ij}/\dot{\gamma} &= \sigma'_{ij}/2\tau \quad \text{if} \quad \dot{\gamma} > 0 \quad \text{and} \quad P > 0 \end{aligned} \quad [2]$$

where, $i, j = 1, 2, 3$. In these equations, $\boldsymbol{\sigma}$ represents the Cauchy stress tensor and $\sigma'_{ij} (= \sigma_{ij} + P\delta_{ij})$ represents the deviatoric part of $\boldsymbol{\sigma}$ where $P (= -\sigma_{ii}/3)$ represents the hydrostatic pressure. $\tau (= \sqrt{\sigma'_{ij}\sigma'_{ij}/2})$ represents the equivalent shear stress and μ_{int} and ρ_c represent the bulk friction coefficient and critical close-packed density of the granular volume. $D_{ij} (= (\partial_i v_j + \partial_j v_i)/2)$ represents the (plastic) flow rate tensor, and $\dot{\gamma} (= \sqrt{2D_{ij}D_{ij}})$ represents the equivalent shear rate. We assume the surface friction coefficient μ_{surf} describes the interaction of the granular continuum with intruder surfaces.

We use a 3D Material Point Method (MPM) solver from Baumgarten and Kamrin (29) to implement the continuum modeling in this study, which has been successfully used for modeling complex problems in the past (29, 30). We have also validated the accuracy of the continuum model against experiments for a specific set of 3D plate intrusions, which justify the use of the continuum solver for generating 3D-RFT reference data. The details of the validation studies are provided in the Methods and Materials section.

3. 3D-RFT premises

We begin by systematically summarizing the physical assumptions and constraints we use to arrive at a generic 3D-RFT (the next section will provide further details on how these premises are used). These premises act as the guiding principles for establishing the form of 3D-RFT and are also useful for understanding the limits of 3D-RFT.

1. **Premise-1: Localization and decoupling of forces** This hypothesis assumes that the force on any sub-surface of an intruding body is independent of the motion or configuration of any other sub-surface of the body. This is the primary order-reduction hypothesis inherent to all RFT’s, e.g. it is used in Eq 1.
2. **Premise-2: Leading-edge hypothesis** This hypothesis assumes that only the *leading edges* of a body (surfaces moving ‘into’ and not ‘away from’ a granular volume) experience non-negligible resistive force. Mathematically, such surfaces have a positive dot product between their surface normal and velocity direction ($\hat{\mathbf{v}} \cdot \hat{\mathbf{n}} \geq 0$). The hypothesis applies only to non-cohesive media. Section S5 in the Supplementary Information provides evidence in support of this hypothesis in three dimensions.

3. **Premise-3: Validity of the continuum model** We suppose that the medium is well-represented by the continuum model shown in Eq 2, which is used to guide the theory for 3D-RFT. This is akin to other advances in RFT stemming from this same basic continuum model (21, 25). Consequently, the resistive force on a plate depends on the same limited set of material parameters that govern the continuum model: ρ_c (the critical density), μ_{int} (the internal friction), and μ_{surf} (the media-surface friction).
4. **Premise-4: Force dependence on material internal friction** We use extensive data analysis to explore the dependence of resistive force on μ_{int} . From this, we assert that the normal force is relatively uninfluenced by μ_{surf} for a large range of internal friction ($\mu_{\text{int}} = 0.3 - 0.9$) (see Fig S2). Between different μ_{int} , the normal forces appear to only vary by a multiplicative scalar factor ξ_n as discussed in Sec 4.
5. **Premise-5: Force dependence on media-intruder surface friction** We use a similar analysis as done in the previous premise to explore the dependence of surface tractions on μ_{surf} . From this, we assert that the tangential forces strongly depend on μ_{surf} . Specifically, we observe that plate-tangential resistive forces generated at a higher μ_{surf} can be used to generate the tangential force for a lower μ_{surf} ; the dependences at the lower surface friction can be obtained by limiting the magnitude of the tangential force based on the Coulomb friction limit at the lower μ_{surf} . Detailed material response graphs in this regard can be found in Sec S3 of the Supplementary Information.
6. **Premise-6: Isotropy of the drag force relation** Any function providing the intrusion force on an intruder must obey a symmetry relationship whereby if the entire problem is rotated by some amount — that is the free-surface, gravity, intruder orientation/position, and intruder velocity are all rotated the same amount — then the resistive force must also rotate by this common global rotation. As we will show, this constraint, which implies the drag force relations are isotropic functions of their inputs, imposes a rather strong restriction on the three-dimensional form that 3D-RFT can take.
7. **Premise-7: Consistency with lower-dimensional RFT** We desire a 3D-RFT model that collapses back to the previously defined 2D-RFT description in the appropriate limits. Thus, in line with the angle-based characterization of 2D-RFT by Li et al. (14) (Fig 1), we desire to ultimately express 3D-RFT in terms of similar characteristic angles β and γ and a new twist angle ψ representing the angle between the planes of plate normal and velocity direction with the vertical.

In addition to the above premises, we will utilize a few operational constraints. We limit ourselves to quasi-static intruder motions, with negligible inertial effects in the granular media. This was also assumed in the original 2D-RFT formulation and lets the force on a sub-surface be deemed independent of the surface's speed. More recently, an inertia-sensitive 2D-RFT has also been proposed and validated (25). We limit our attention to quasi-static cases in this work (See Materials and Methods section for more details). We also

require that intruders are only submerged to a shallow depth. This comes from limits on the linearity of granular material's resistance with depth $|z|$ in a gravity-loaded system and limits us to considering depths only up to a $O(1)$ factor of the size of the object being intruded (24, 31). Lastly, the RFT form assumes grains to be small relative to the size-scale of the intruder. RFT is expected to have reduced accuracy along intruder surfaces that sharply vary; direct grain-size effects may be important to determining the resistive force on these subsurfaces.

4. Proposed form of 3D-RFT

In light of Premise 1, we propose a 3D-RFT taking the following form:

$$\mathbf{F}_{\text{total}} = \int_{\text{surf}} \boldsymbol{\alpha}^{\text{mat}}(\hat{\mathbf{n}}, \hat{\mathbf{v}}, \mathbf{g}) |z| ds. \quad [3]$$

Here, the $\boldsymbol{\alpha}^{\text{mat}}$ function is expressed in terms of three vectors, the outward surface normal $\hat{\mathbf{n}}$, velocity direction $\hat{\mathbf{v}}$, and gravity \mathbf{g} . Note that 2D-RFT could be expressed equally well in this form.

In particular, referring to Premise 3, we write

$$\boldsymbol{\alpha}^{\text{mat}}(\hat{\mathbf{n}}, \hat{\mathbf{v}}, \mathbf{g}) = \boldsymbol{\alpha}(\hat{\mathbf{n}}, \hat{\mathbf{v}}, \mathbf{g}; \rho_c, \mu_{\text{int}}, \mu_{\text{surf}}). \quad [4]$$

Further, we assume the force per area per depth can be decomposed into normal and tangential parts with the following property dependences, which align with Premises 4 and 5:

$$\boldsymbol{\alpha} = \boldsymbol{\alpha}_n(\hat{\mathbf{n}}, \hat{\mathbf{v}}, \mathbf{g}; \rho_c, \mu_{\text{int}}) + \boldsymbol{\alpha}_t(\hat{\mathbf{n}}, \hat{\mathbf{v}}, \mathbf{g}; \rho_c, \mu_{\text{int}}, \mu_{\text{surf}}), \quad [5]$$

where $\boldsymbol{\alpha}_n$ and $\boldsymbol{\alpha}_t$ represent normal and tangential contributions to $\boldsymbol{\alpha}$. We propose the following simplifying functional forms consistent with Premises 4 and 5

$$\boldsymbol{\alpha}_n = \rho_c g \hat{f}(\mu_{\text{int}}) |\boldsymbol{\alpha}_n^{\text{gen}}(\hat{\mathbf{n}}, \hat{\mathbf{v}}, \hat{\mathbf{g}})| (-\hat{\mathbf{n}}) \quad [6]$$

$$\boldsymbol{\alpha}_t = \rho_c g \hat{f}(\mu_{\text{int}}) \min\left(\frac{\mu_{\text{surf}} |\boldsymbol{\alpha}_n^{\text{gen}}(\hat{\mathbf{n}}, \hat{\mathbf{v}}, \hat{\mathbf{g}})|}{|\boldsymbol{\alpha}_t^{\text{gen}}(\hat{\mathbf{n}}, \hat{\mathbf{v}}, \hat{\mathbf{g}})|}, 1\right) \boldsymbol{\alpha}_t^{\text{gen}}(\hat{\mathbf{n}}, \hat{\mathbf{v}}, \hat{\mathbf{g}}). \quad [7]$$

The prefactor $\rho_c g \hat{f}(\mu_{\text{int}})$, which we collectively refer to as ξ_n , is a media dependent scaling coefficient reflecting the overall intrusive strength of the system. The presence of the multiplicative ρg factor is required on dimensional grounds (21). Additionally, we find that \hat{f} follows a roughly cubic dependence on μ_{int} (see Fig S3 in Supplementary Information for more details). This dependence is in accord with the observations of many researchers in the past in simpler vertical intrusions of flat plates in granular volumes (a sub-case of 3D-RFT)(32). Section S2 of Supplementary Information provides the detailed material response graphs in this regard.

The *generic* RFT functions shown with superscript 'gen' are labeled as such because we model them to be approximately universal across all granular/intruder systems. The min function in the formula for $\boldsymbol{\alpha}_t$ acts as a cut-off that ensures the ratio of tangential and normal force on a plate element does not exceed the media-surface friction coefficient μ_{surf} , as per Premise 5.

The largest meaningful value of μ_{surf} is $\mu_{\text{surf}} = \mu_{\text{int}}$, which is the fully-rough limit wherein the min function is always 1. In this case, we have $\boldsymbol{\alpha} = \xi_n \boldsymbol{\alpha}^{\text{gen}}$ where

$$\boldsymbol{\alpha}^{\text{gen}} \equiv \boldsymbol{\alpha}_n^{\text{gen}} + \boldsymbol{\alpha}_t^{\text{gen}}. \quad [8]$$

The 3D-RFT model we are proposing is closed upon choosing the scalar-valued function \hat{f} and the vector valued function α^{gen} . Upon selection of these two functions, Eqs 6 and 7 can be used to determine α , and hence α^{mat} , for any choice of μ_{int} and μ_{surf} .

Symmetry constraints on 3D-RFT formulation. We use symmetry constraints inherent to the drag problem (Premise 6) to constrain the functional form of α^{gen} . Our strategy is to constrain the function space to satisfy symmetry constraints *by design* rather than leaving it to chance based on the choice of fit functions. Moreover, by enforcing the symmetry constraints directly, we reduce the space of admissible functions, thereby reducing the amount of fitting that must be done.

Consider a small plate intruder characterized with \hat{n} , \hat{v} , ds , $|z|$, and \hat{g} . For $\mu_{\text{surf}} = \mu_{\text{int}}$, the force on the plate according to RFT is $d\mathbf{f} = \xi_n \alpha^{\text{gen}}(\hat{n}, \hat{v}, \hat{g})|z|ds$. If the entire system is rotated — including the intruder, the granular bed, and gravity — the resistive force on the intruder must rotate by the same amount. This is because rotating the entire system should be consistent with a fixed system and a rotation of the observer. Figure 3A visualizes this action. Thus, for any rotation \mathbf{R} , we expect that $\mathbf{R}d\mathbf{f} = \xi_n \alpha^{\text{gen}}(\mathbf{R}\hat{n}, \mathbf{R}\hat{v}, \mathbf{R}\hat{g})|z|ds$, and thus

$$\alpha^{\text{gen}}(\mathbf{R}\hat{n}, \mathbf{R}\hat{v}, \mathbf{R}\hat{g}) = \mathbf{R}\alpha^{\text{gen}}(\hat{n}, \hat{v}, \hat{g}). \quad [9]$$

This ‘global rotation constraint’ implies α^{gen} is an isotropic function of its inputs. Thus, in accord with Isotropic Representation Theory (IRT)(33) the function must have the following specific form:

$$\alpha^{\text{gen}}(\hat{n}, \hat{v}, \hat{g}) = f_1 \hat{n} + f_2 \hat{v} + f_3 \hat{g}, \quad [10]$$

where f_1 , f_2 , and f_3 are three mutually-independent arbitrary scalar-valued functions of coordinate-invariant *dot-products* between the three direction vectors, that is $f_i = f_i(\hat{g} \cdot \hat{v}, \hat{g} \cdot \hat{n}, \hat{n} \cdot \hat{v})$. Equation 10 has reduced the problem of fitting α^{gen} from determining a vector-valued function of six independent variables (three vectors with unital constraints) to determining a vector-valued function of three independent variables (three dot products). Note that the form given in Eqs 6-7 for general μ_{surf} continues to satisfy the IRT requirement Eq 10. A detailed proof in this regard is provided in section S3 of the Supplementary Information.

We next introduce the methodology for parametrizing sub-surfaces in terms of three angles to arrive at our ultimate description of α^{gen} .

3D-RFT sub-surface characterization.

Use of a local coordinate frame. Equations 6-10 define the stresser-depth on a sub-surface using \hat{n} , \hat{v} , and \hat{g} directions (beside material properties). We define a local cylindrical coordinate system at each sub-surface based on its local velocity (\hat{v}) and gravity direction (\hat{g}). We choose the direction opposite to the gravity (upward in general) as the positive z -direction and use the horizontal component of \hat{v} as the positive \hat{r} direction. The remaining $\hat{\theta}$ direction is chosen as the cross product between \hat{r} and \hat{z} . The free-surface is taken as the reference ($z = 0$) for the z -direction.

$$\begin{aligned} \text{local } z\text{-direction : } \hat{z} &= -\hat{g} \\ \text{local } r\text{-direction : } \hat{r} &= \frac{\mathbf{v} - (\mathbf{v} \cdot \hat{z})\hat{z}}{|\mathbf{v} - (\mathbf{v} \cdot \hat{z})\hat{z}|} \\ \text{local } \theta\text{-direction : } \hat{\theta} &= \hat{z} \times \hat{r} \end{aligned} \quad [11]$$

When $|\mathbf{v} - (\mathbf{v} \cdot \hat{z})\hat{z}|$ is zero (a sub-surface moves up or down), \hat{r} is set to the direction of the horizontal component of the surface-normal i.e. $\hat{r} = (\hat{n} - (\hat{n} \cdot \hat{z})\hat{z})/|\hat{n} - (\hat{n} \cdot \hat{z})\hat{z}|$.

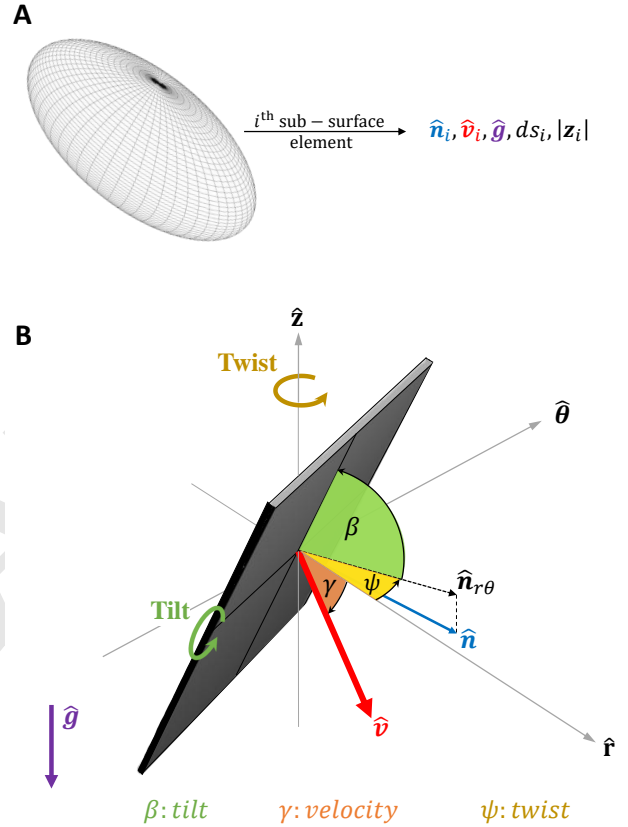


Fig. 2. 3D-RFT surface element characterization: (A) Any moving sub-surface is represented using surface normal (\hat{n}), area magnitude (ds), depth ($|z|$), velocity direction (\hat{v}), and gravity direction (\hat{g}). (B) Directions \hat{n} and \hat{v} are expressed using three characteristic angles — plate tilt (β , green), plate twist (ψ , yellow), and velocity angle (γ , orange) in the local coordinate frame $\{\hat{r}, \hat{\theta}, \hat{z}\}$. The functional forms of these angles and local coordinate frame are given in Eq 11 and 16-18.

Next, in line with Premise 7, we recast Eq 10 in terms of angles β , γ , and ψ and directions $\{\hat{r}, \hat{\theta}, \hat{z}\}$. Usage of characteristic angles $\{\beta, \gamma, \psi\}$ (described next) helps us meet our desire to maintain a consistency of 3D-RFT with the 2D-RFT form (Premise 7). Secondly, unlike $\{\hat{n}, \hat{v}, \hat{g}\}$, $\{\hat{r}, \hat{\theta}, \hat{z}\}$ represent an orthogonal co-ordinate frame. Use of this choice eases the physical interpretation of the components of α^{gen} , which is helpful for potential applications based on 3D-RFT, and simplifies model calibration.

Sub-surface orientations. : We use the sub-surface’s normal direction \hat{n} to characterize its orientation in the local coordinate frame. We use two angles, the angle of twist (ψ) and the angle of tilt (β) for this characterization. See figure 2B for a visual representation of ψ and β .

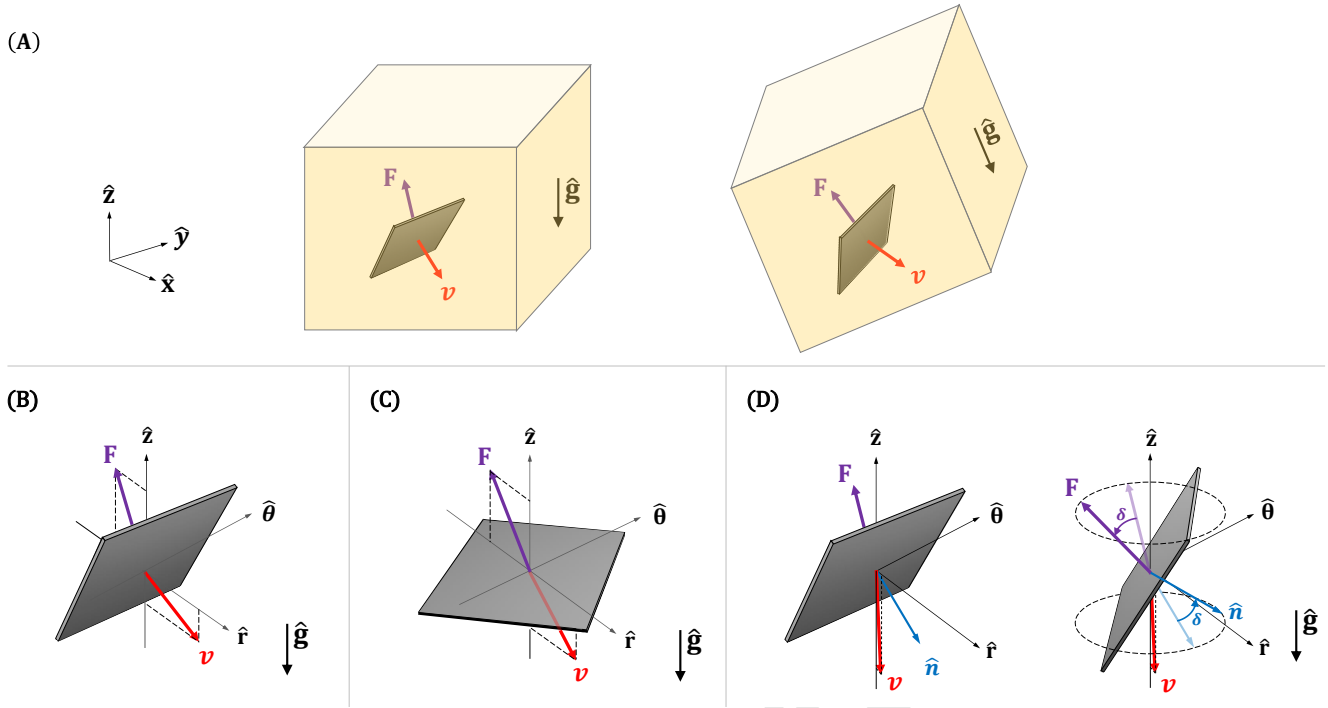


Fig. 3. 3D-RFT symmetry constraints: (A) Global rotational constraint requiring the drag force to be an isotropic function of the plate normal, motion direction, and gravity direction. Some consequences of this constraint are *plate twist symmetry*, *plate tilt symmetry*, and *vertical motion symmetry*. (B) A special case of *plate twist symmetry*: $F_\theta(\beta, \gamma, \psi = 0) = 0$. (C) A special case of *plate tilt symmetry*: $F_\theta(\beta = 0, \gamma, \psi) = 0$, and (D) *Vertical motion symmetry*: $(\beta, \gamma = \pm\pi/2, \psi = 0) \rightarrow (\beta, \gamma = \pm\pi/2, \psi = \delta)$ causes $(F_r, F_\theta = 0, F_z) \rightarrow (F_r \cos \delta, F_r \sin \delta, F_z)$. Violet, red, and blue arrows show force, velocity, and surface-normal direction, respectively.

Surface twist angle (ψ): We define ψ as the azimuthal angle between the r -axis and the projection of the surface normal onto the $r\theta$ -plane, denoted by $\hat{n}_{r\theta}$.

Surface tilt angle (β): We define β as the polar angle between the r -axis and the $r\theta$ -plane. To be clear, β measures the angle between the $r\theta$ -plane and one of \hat{n} or $-\hat{n}$, whichever gives a result in the $[-\pi/2, \pi/2]$ range. This choice is not problematic because at any time, only one side of a plate element experiences forces, and this can be identified using the leading edge condition ($\hat{v} \cdot \hat{n} \geq 0$) of Premise 2 which guarantees $\beta \in [-\pi/2, \pi/2]$.

Next we describe the representation of the velocity direction.

Angle of attack (γ): The local coordinate frame definitions (Eq 11) keep the velocity vector completely within the rz -plane. Thus, once $\{\hat{r}, \hat{\theta}, \hat{z}\}$ are determined, only one angle is needed to represent the velocity direction. We call this angle γ ; see Fig 2B. We define γ as the angle between the velocity direction vector and the local positive r -axis.

Based on the above definitions, the variations of each of the system characteristic angles $\{\beta, \gamma, \psi\}$ is restricted to $[-\pi/2, \pi/2]$ for any leading-edge surface. We use these limits in the generation of reference 3D-RFT data. Mathematical formulas for the angles in terms of vector components in a fixed cartesian frame are provided in the Material and Methods section.

We express the final form of α^{gen} in the local coordinate frame $\{\hat{r}, \hat{\theta}, \hat{z}\}$ by expressing $\{\hat{n}, \hat{v}, \hat{g}\}$ as:

$$\begin{aligned} \hat{g} &= -\hat{z}, & \hat{v} &= \cos \gamma \hat{r} - \sin \gamma \hat{z} \\ \hat{n} &= \sin \beta \cos \psi \hat{r} + \sin \beta \sin \psi \hat{\theta} - \cos \beta \hat{z} \end{aligned} \quad [12]$$

Substitution of definitions in Eq 10 gives the expressions for the r , θ , and z components of α^{gen} as follows:

$$\alpha^{\text{gen}} = \alpha_r^{\text{gen}} \hat{r} + \alpha_\theta^{\text{gen}} \hat{\theta} + \alpha_z^{\text{gen}} \hat{z} \quad [13]$$

$$\alpha_r^{\text{gen}}(\beta, \gamma, \psi) = f_1 \sin \beta \cos \psi + f_2 \cos \gamma$$

$$\alpha_\theta^{\text{gen}}(\beta, \gamma, \psi) = f_1 \sin \beta \sin \psi$$

$$\alpha_z^{\text{gen}}(\beta, \gamma, \psi) = -f_1 \cos \beta - f_2 \sin \gamma - f_3 \quad [14]$$

where, $f_1 = f_1(x_1, x_2, x_3)$, $f_2 = f_2(x_1, x_2, x_3)$, and $f_3 = f_3(x_1, x_2, x_3)$ are three functions of $\{x_1, x_2, x_3\}$ defined as:

$$\begin{aligned} x_1 &= \hat{g} \cdot \hat{v} = \sin \gamma, & x_2 &= \hat{g} \cdot \hat{n} = \cos \beta, \\ x_3 &= \hat{n} \cdot \hat{v} = \cos \psi \cos \gamma \sin \beta + \sin \gamma \cos \beta. \end{aligned} \quad [15]$$

The 3D-RFT model we introduce is closed upon fitting the three functions $f_i(x_1, x_2, x_3)$. Note that by building the functional relationships for α_r^{gen} , $\alpha_\theta^{\text{gen}}$, and α_z^{gen} from IRT (Eq 14), the model automatically satisfies many *easy-to-observe* local constraints regardless of the choice of the f_i 's. These constraints include (i) '*plate twist symmetry*' (Fig 3B), which requires that the sub-surface forces in the r - and z -direction should be even functions of plate twist (ψ), and that force in the θ -direction should be an odd function of ψ ; (ii) '*plate tilt symmetry*' (Fig 3C) which requires that when the plate faces upwards or downwards ($\beta = 0$), the sub-surface force in the θ -direction should vanish, the force magnitude should depend only on γ , and the twist angle ψ should have no influence on the force; and (iii) '*vertical motion symmetry*' (figure 3D), which requires that for any tilt β , as $\gamma \rightarrow \pm\pi/2$ (approaching an upward or downward motion) then any azimuthal rotation (changing ψ at constant β) of a sub-surface should rotate the resultant force on the sub-surface by the same angle.

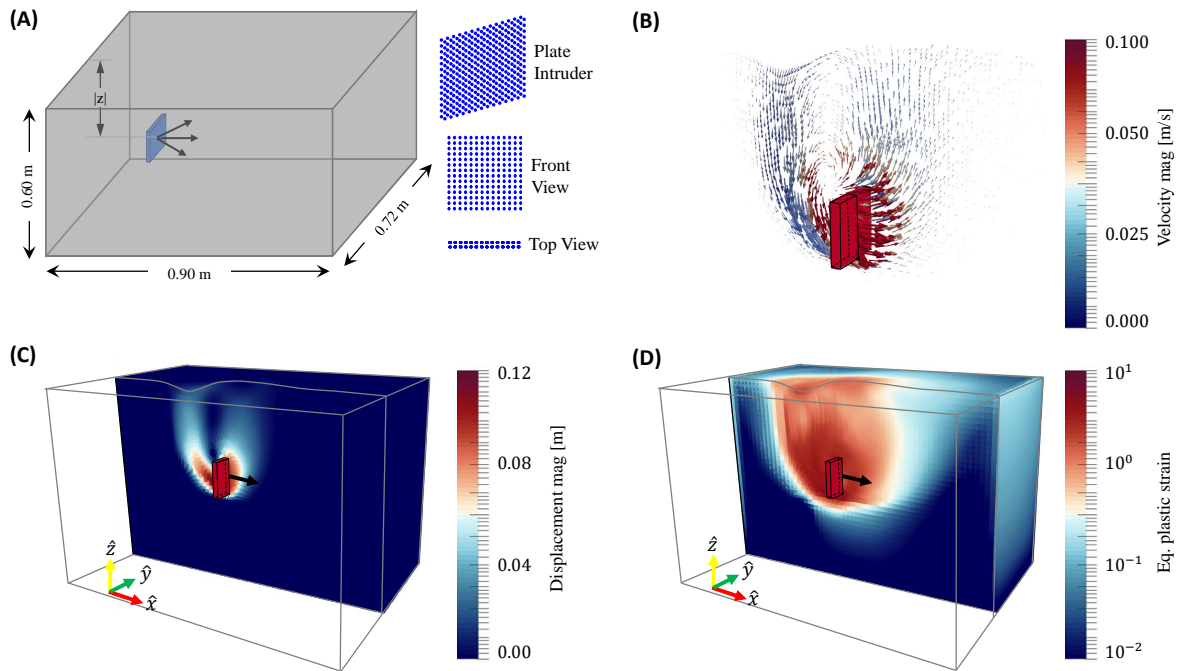


Fig. 4. Reference data collection for 3D-RFT: (A) We use a thin plate (0.105m×0.105m×0.015m) intrusion setup as shown in the schematic for reference data collection for 3D-RFT. We use material point method (MPM) based continuum modeling for data collection. We run 13 combinations of plate tilt angle ($\beta = -\pi/2 : \pi/6 : \pi/2$ rad), 13 combinations of velocity direction angle ($\gamma = -\pi/2 : \pi/6 : \pi/2$ rad), and 7 combinations of plate twist angle ($\psi = 0 : \pi/6 : \pi/2$). (B) material flow, (C) displacement magnitude, and (D) equivalent plastic strain magnitude variation from one of the test setups. Material properties are provided in Appendix-1

5. Reference data

We use a large number of combinations (~ 3000) of material properties ($\rho, \mu_{\text{int}}, \mu_{\text{surf}}$) and 3D-RFT angles (β, γ, ψ) to generate continuum modeling-based reference data for evaluating the 3D-RFT form. The details of the combinations are provided in the Materials and Methods section. Polynomial fits for f_1, f_2 , and f_3 are provided in the Supplementary Information (Table S3 and table S4). Figure 4 shows the simulation setup used for the data collection. While both the β and the γ angles are varied over the interval $[-\pi/2, \pi/2]$, ψ was varied only in $[0, \pi/2]$ taking advantage of ‘plate twist symmetry’ discussed earlier.

Figure 5 shows an example of 3D-RFT fittings against reference data. Odd columns in the figure show the data obtained using continuum simulations as a function of β and γ at four ψ values. The material properties were $\mu_{\text{int}} = 0.4$, $\rho_c = 3000 \text{ kg/m}^3$, and $\mu_{\text{surf}} = 0.15$. Corresponding 3D-RFT fittings are plotted on the even columns. We find the value of the scaling coefficient ξ_n to be $0.92 \times 10^6 \text{ N/m}^3$ for this material. While Eq 14 represents the most generic form of 3D-RFT, the choice of the $f_i(x_1, x_2, x_3)$ determines the final 3D-RFT form. All the results presented in this work use 3rd degree polynomial fits for the f_i in $\{x_1, x_2, x_3\}$ (Table S3). Higher-order polynomials could be used, which can better fit the reference data. We provide one such form in the Supplementary Information (Table S4). The performance of 3D-RFT does not change significantly between 3rd and 4th degree polynomial fits. The latter form fits the trends of $|\alpha_t|/|\alpha_n|$ better but has inconsequential effects on 3D-RFT predictions for the test cases used in this study.

The 3D-RFT model we propose is summarized by Eqs 3-8, with \hat{f} fit as shown in Fig S3, and with α^{gen} expressed

using Eqs 12-14 in terms of third degree polynomial fits for the f_i , and using directions $\{\hat{r}, \hat{\theta}, \hat{z}\}$ and angles $\{\beta, \gamma, \psi\}$ as shown in Fig 4. To numerically implement the model, we discretize the intruder surface into small plate elements and determine $\{\beta, \gamma, \psi\}$ and $\{\hat{r}, \hat{\theta}\}$ for each element. The model then provides the force on each element that is on the leading edge of the intruder. A step-by-step implementation strategy for 3D-RFT is given in the Materials and Methods section.

6. Validation studies

We first test the accuracy of the implied localization rule (Premise 1) of the proposed form of 3D-RFT by comparing its predictions for ten arbitrary intruding objects to full continuum model solutions of the same intrusions. We use the material properties $\mu_{\text{int}} = 0.4$, $\rho_c = 3000 \text{ kg/m}^3$, and $\mu_{\text{surf}} = 0.4$ for these cases. A representation of the objects and their dimensions are provided in Fig 6 and its caption. The object length scales are kept to be 7 cm in all the cases, and the objects are submerged to an initial depth of 27 cm (vertical distance between the free surface and the geometric center of the shape). The objects are moved at a speed of 0.1 m/s in different directions in the xz -plane. These directions are characterized using θ , which represents the angle between the velocity direction (\hat{v}_θ) and the positive x -axis in a clockwise direction (same as γ definition for a plate element). Negative θ represents upward motion, positive θ represents downward motion, and $\theta = 0$ represents horizontal motion along the x -direction. The variations of net-force (F_x, F_y , and F_z) with θ are plotted in Fig 6. 3D-RFT agrees with the continuum solutions well in modeling all the intrusion test scenarios considered in Fig 6. Objects with sharp corners generally show somewhat weaker fits than those with smoother shapes; this

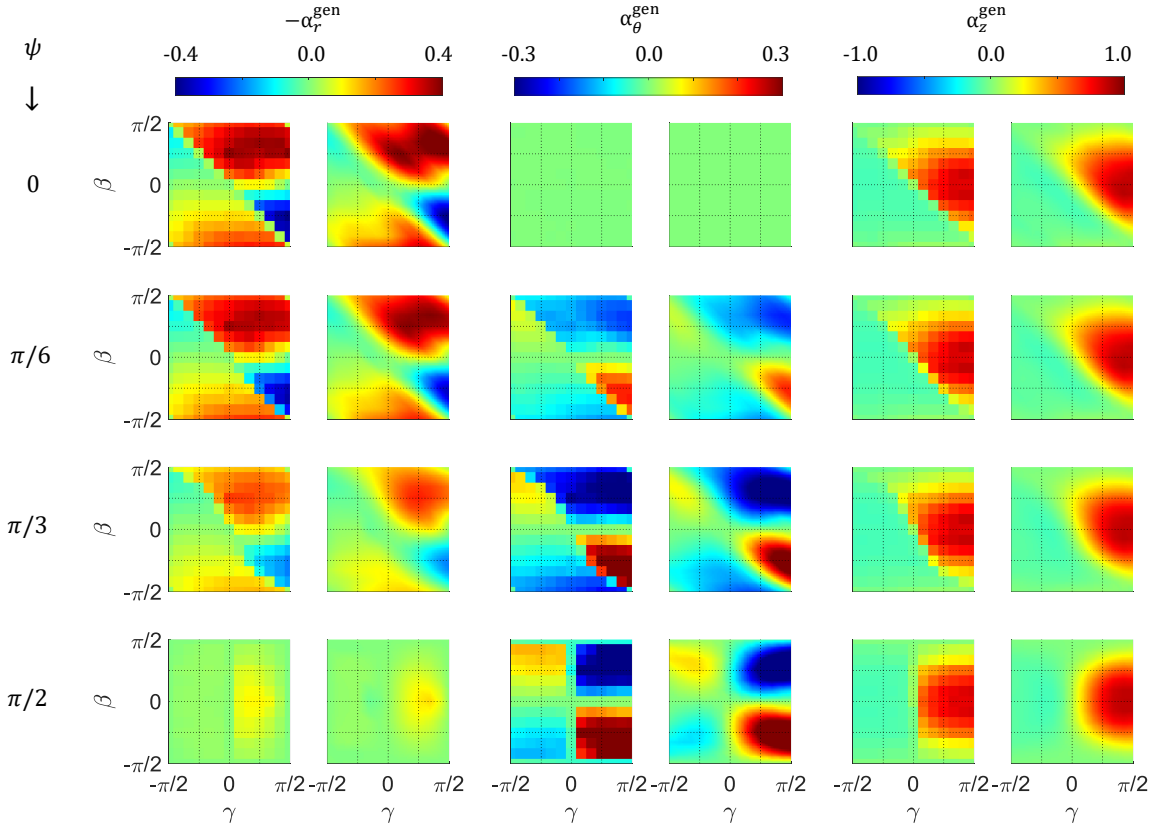


Fig. 5. Sample 3D-RFT fittings: Reference normalized forces ($F/A|z|\xi_n$) and functional fittings (right) for plate intrusions at various plate twists ($\psi = [0, \pi/6, \pi/3, \pi/2]$ rad), plate inclinations ($\beta = -\pi/2 : \pi/6 : \pi/2$ rad), and velocity directions ($\gamma = -\pi/2 : \pi/6 : \pi/2$ rad) for a material with $\mu_{\text{int}} = 0.4$, $\rho = 3000 \text{ kg/m}^3$, and $\mu_{\text{surf}} = 0.15$. The reference data is normalized with $\xi_n = 0.92 \times 10^6 \text{ N/m}^3$.

could be because sharp corners are difficult to represent with our material point method.

Validation of 3D-RFT with detailed DEM studies. We further check the performance of 3D-RFT with two DEM studies. In these studies, we measure net moment, net force, and resistive force distribution on bodies intruding into granular volumes with simultaneous rotation and translation velocities. We use a 50/50 mixture of 3 mm and 3.4 mm diameter (d) grains with a grain density of 2470 kg/m^3 and the granular volumes have an effective bulk density of 1310 kg/m^3 ($\phi \approx 0.53$) in both the DEM studies. We determine the internal coefficient of friction μ_{int} as 0.21 using simple shear simulations. Section S6 of the Supplementary Information provides more details of the simple shear test setup and detailed material properties. We use a scaling coefficient (ξ_n) value of $0.12 \times 10^6 \text{ N/m}^3$ based on the \hat{f} relationship between $\xi_n/\rho_c g$ and μ_{int} shown in Fig S3. See Table S1 and section S1 for more details.

Cylinder Drill: In this test, we model simultaneous rotation and translation (drilling) of a *solid cylindrical* intruder along the z -axis in a granular volume (diameter= 0.05 m, length=0.14 m). The setup consists of approximately 6×10^5 particles in a $100d \times 100d \times 70d$ sized granular bed. The setup dimensions and setup schematic are provided in Fig 7. The figure also shows the variations of force and moment on the intruder over time from the DEM studies versus 3D-RFT. In addition, the figure shows the variation of stress over the

intruder surface from DEM and 3D-RFT. All reported components (net force and moments, as well as stress distributions) show a strong match between the two approaches.

Bunny Drill: In this test, we model the drilling motion ($\omega = 2\pi \text{ rad/s}$, $v = 0.1 \text{ m/s}$) of a *Stanford Bunny* (34) shaped rigid intruder in a granular volume. The shape is chosen because it is an example of a complex, asymmetric 3D object. The granular bed consists of approximately 2.1×10^6 particles spread over a $150d \times 150d \times 88d$ sized domain. The bunny shape was slightly modified from the standard shape — the shape was proportionally scaled in such a way that the bunny height measures 0.1 m, and the bunny base was flattened to make the base a plane surface without an inward extrusion. Figure 8 shows the simulation setup where the grains are colored with velocity magnitudes. Figure 8 also shows the variation of stresses over the intruder surface from DEM and 3D-RFT. All the reported components (net force and moments, as well as stress distributions) show a strong match between the two approaches.

7. Conclusion

3D-RFT is an important step towards developing a generic real-time modeling technique capable of modeling granular intrusion of arbitrarily shaped objects over a large range of low and high-speed scenarios in diverse materials and environments. Previously, granular RFT's usage has focused on the modeling of arbitrary 2D objects moving in-plane. We

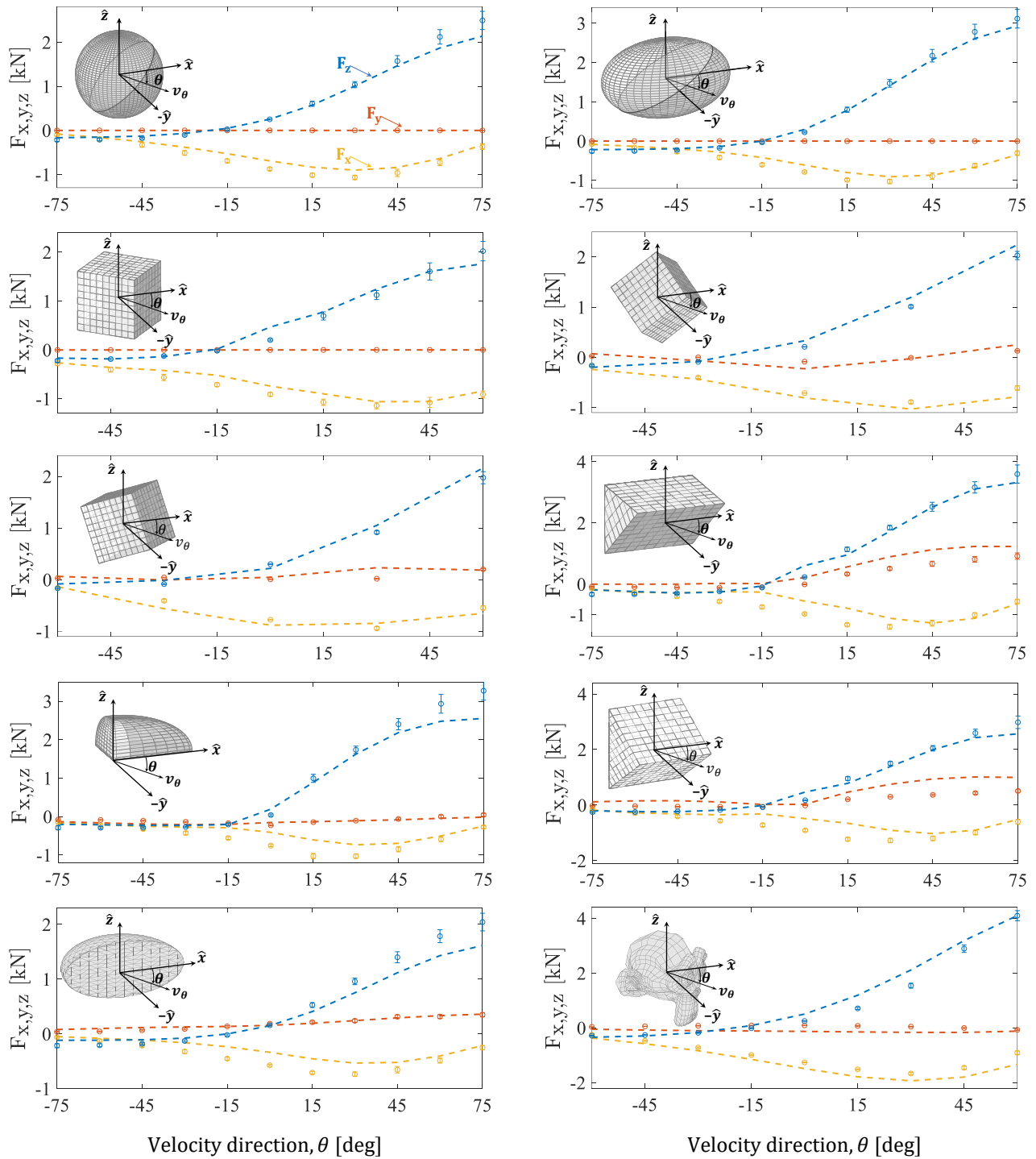


Fig. 6. 3D-RFT Verification Studies 1-10: Variation of different force components (F_x : yellow, F_y : orange, and F_z : blue) during motions of various rigid objects (intruders) obtained from continuum modeling ('o' markers) and 3D-RFT (dashed lines) at various velocity directions (\hat{v}_θ). All the studies were conducted at a velocity magnitude of 0.1 m/s. θ represents the angle between \hat{v}_θ and the positive x -axis. All the velocities completely lie in the xz -plane. A pictorial representation of each intruder is provided in the corresponding sub-figure. The intruder shapes include (1) a 5 cm radius sphere, (2) an ellipsoid with [7.5, 4.5, 4.5] cm semi-axes (x, y, z), (3) a 7.5 cm tilted cube, rotated from a cartesian alignment by $\pi/4$ radians about the z -axis, (4) a 7.5 cm cube sequentially rotated by $\pi/3$ and $\pi/4$ radians along the y -axis and z -axis from a cartesian alignment, (5) a 7.5 cm cube sequentially rotated by $\pi/6$ and $\pi/3$ radians along the y -axis and z -axis from a cartesian coordinate alignment, (6) an isosceles right angle prism with 7.5 cm equal sides and 10.5 cm width, (7) a quarter ellipsoid with [7.5, 4.5, 4.5] cm semi-axes (x, y, z) ($x > 0$ and $y > 0$), (8) an isosceles right angle prism with equal sides of 10.5 cm and 7.5 cm width, (9) a half-ellipsoid with [7.5, 4.5, 4.5] cm semi-axes (x, y, z) ($y > 0$), and (10) a monkey head shape from the open-source 3D computer graphics software 'Blender' at a scale factor of 0.075 and facing $\pi/4$ radians from the positive x -direction in the xy -plane.

have proposed an extension of RFT to three dimensions in a fashion consistent with granular continuum mechanics and

necessary symmetry constraints. The accuracy of the proposed 3D-RFT was demonstrated against a variety of full-field

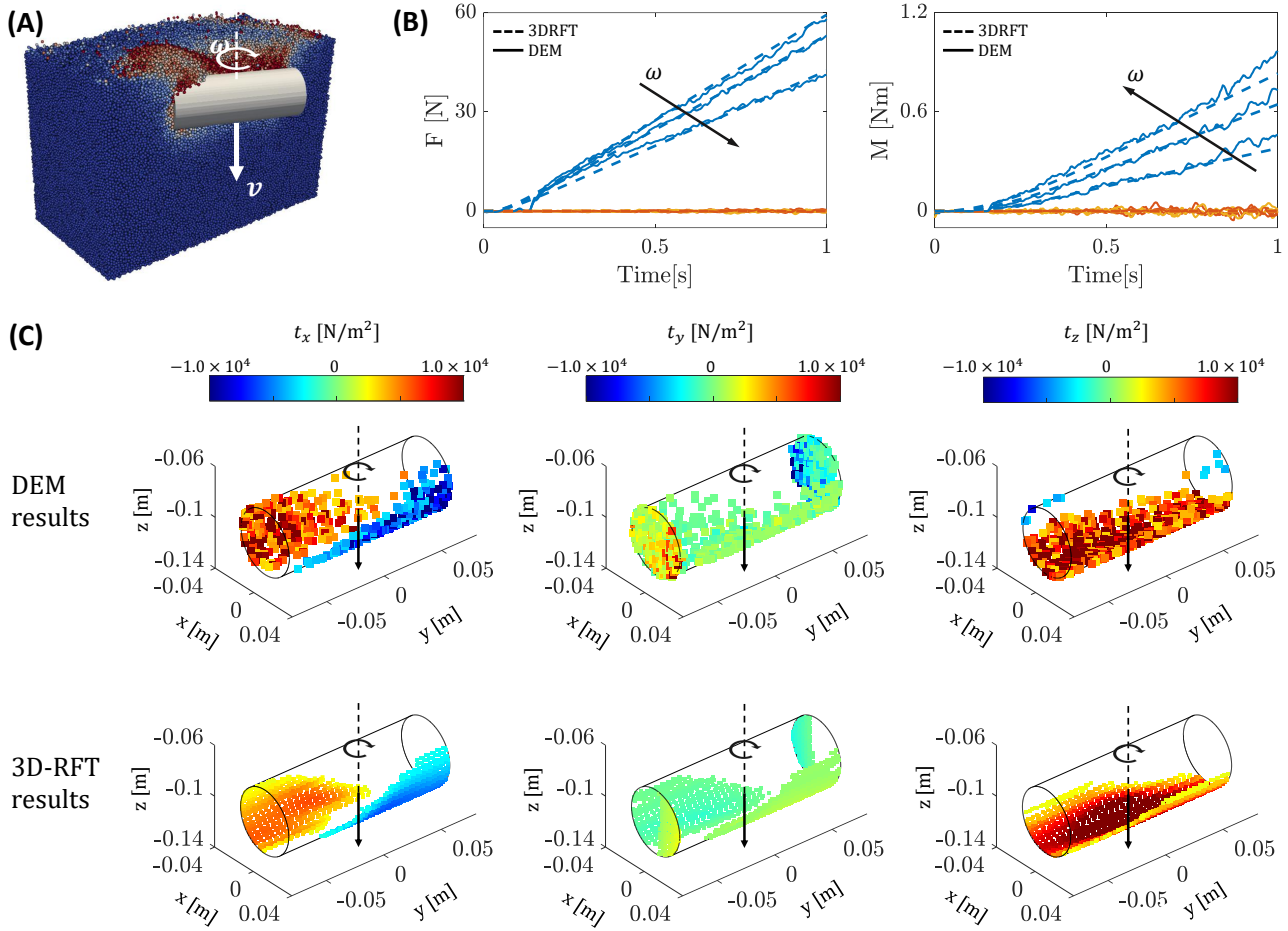


Fig. 7. DEM based 3D-RFT verification: Cylinder drill: (A) A snapshot of the cylinder drill setup where a 50 mm diameter and 140 mm length cylinder was simultaneously rotated (ω , clockwise) and translated (v , downwards) along the z -axis. We use three combinations of (ω, v) : $[(0.25\pi, 0.1), (0.5\pi, 0.1), (\pi, 0.1)]$ (rad/s,m/s). Black arrows in (B) show the direction of increasing ω in each graph. The grains are colored with velocity magnitudes. The simulation domain consisted $\sim 6 \times 10^5$ particles (50/50 mix of 3 mm and 3.4 mm diameter (d) grains) spread over $100d \times 100d \times 70d$ physical space. (B) Variation of net force (F , left) and moment (M , right) components (x : yellow, y : orange, and z : blue) from DEM (solid lines) and 3D-RFT (dotted lines) for $\omega = \pi$ rad/s. (C) Variation of various force components from DEM (Top) and 3D-RFT (Bottom) at a 10 cm depth below the free surface ($t = 1$ s). The DEM material properties are provided in table S2 of the Supplementary Information.

intrusion simulations, both continuum and DEM. Notably, we provide a scheme that determines 3D-RFT in different intrusion systems quickly and directly in terms of basic properties of the granular media (ρ_c and μ_{int}) and the intruder surface (μ_{surf}). The most immediate opportunity to expand 3D-RFT would be to combine 3D-RFT with Dynamic RFT (25) to build a high-speed three-dimensional RFT (3D-DRFT). The current form of 3D-RFT does not include a “shadowing effect” i.e. the fact that forces are reduced on leading edge surfaces that lie in the immediate wake behind another part of the intruder (35). Such effects are more pronounced in intruders with complex shapes or fine geometric features such as the Bunny shape we consider in this study. Characterizing this effect would be an important addition to RFT. Effects of multi-body intrusions (24, 36), density variations (37), inertial and non-inertial velocity effects (3, 25, 38), cohesion (39, 40), and inclined domains (41) on the resistive forces experienced by intruding bodies are among other aspects for further exploration toward the ultimate goal of a generic and fast granular intrusion model applicable to terradynamical motions (8), granular

impact systems (42, 43), locomotors (44), and many other similar applications. This work also presents a systematic approach towards developing reduced-order models in other similar systems with a combination of mathematical analysis and experiments/simulation-based data collection.

Materials and Methods

Evaluation of quasi-static conditions in a system. We use the following definitions of the micro-inertial number I and the macro-inertial number I_{mac} for evaluating the applicability of 3D-RFT in modeling the granular resistive forces in a granular intrusion system;

$$I = \dot{\gamma} / \sqrt{P / \rho_g d^2}, \quad I_{\text{mac}} = v / \sqrt{P / \rho_g},$$

where $\dot{\gamma}$ represents the material shear rate, P represents the hydrostatic pressure, ρ_g represents the material grain density, d represents the mean grain diameter, and v represents the speed. The I_{mac} formulation is equivalent to the inverse square root of the *Euler number* which measures the ratio of the dynamic pressure ρv^2 to the total pressure P .

The macro- and micro-inertial numbers are defined pointwise within a granular media so, to determine if an intrusion is quasi-

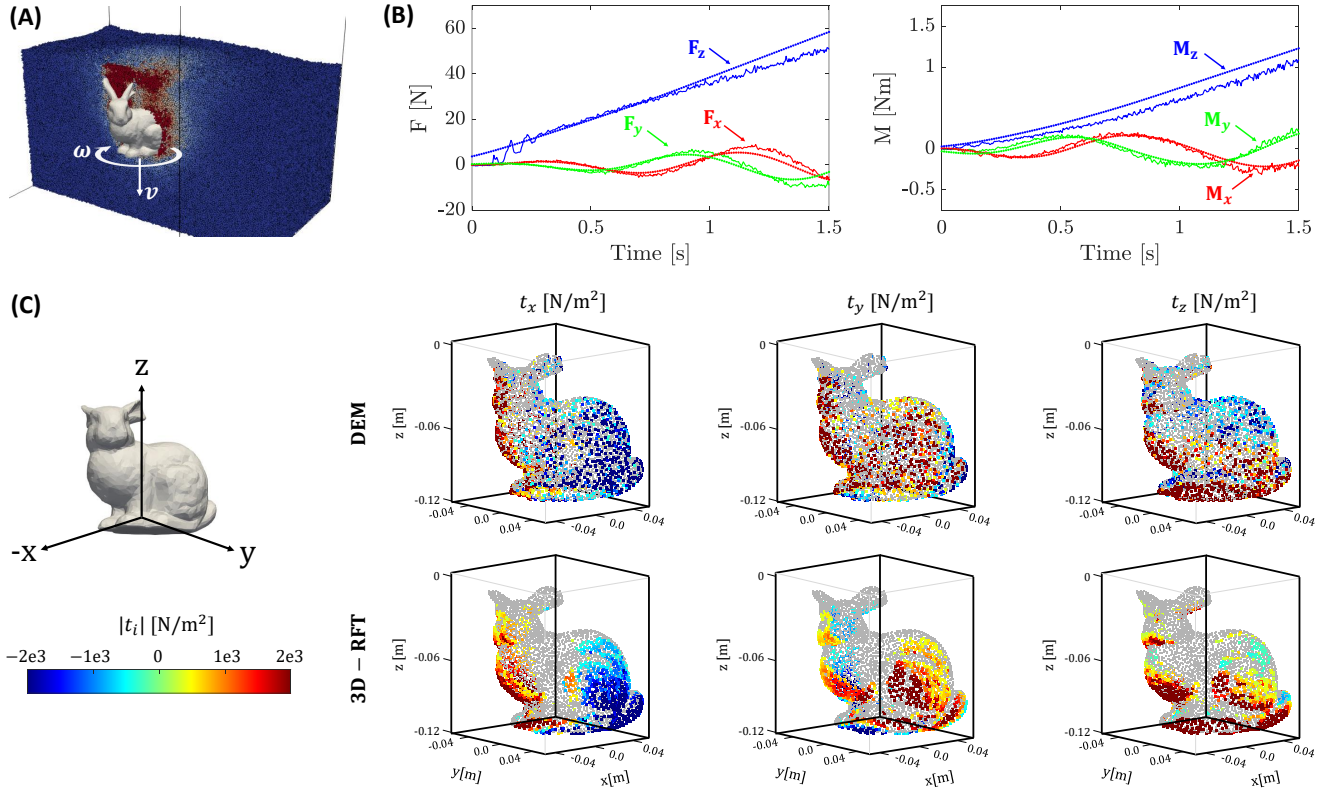


Fig. 8. DEM based 3D-RFT verification: Bunny drill: (A) A snapshot of the Stanford-Bunny drill setup where a 10 cm high stanford-bunny was simultaneously rotated ($\omega = 2\pi\text{rad/s}$, clockwise) and translated ($v = 0.1\text{m/s}$, downwards) along the z -axis. The grains are colored with velocity magnitudes. The simulation domain consisted of $\sim 2.1 \times 10^6$ particles (50/50 split of 3 mm and 3.4 mm diameter (d) grains) spread over a $150d \times 150d \times 88d$ physical space. (B) Variation of net force (F , left) and moment (M , right) components (x : yellow, y : orange, and z : blue) from DEM (solid lines) and 3D-RFT (dotted lines). (C) Commonponents of the surface stress distribution from DEM (Top) and 3D-RFT (Bottom) at a 5 cm bunny-center-depth below the free surface. The DEM material properties are provided in Table S2 of the Supplementary Information.

static, it is convenient to determine characteristic values for these numbers. For this, we use characteristic values of $\dot{\gamma}$, P , and v . We assume that the intruder has an angular velocity ω , a translational velocity v_{intru} , and a characteristic length L . We also assume that the media has a critical density ρ_c and that the system is acted upon by gravity g . We characterize v as $v = \max(v_{\text{intru}}, L\omega/2)$ and $\dot{\gamma}$ as $\dot{\gamma} = v/L$. We consider intrusive loading of the system at characteristic depth L to give a characteristic P as $\xi_n L$. Upon substitution, we get:

$$I \sim (v/L)/\sqrt{(\xi_n L)/\rho_g d^2} = \sqrt{\frac{v^2 \rho_g d^2}{\xi_n L^3}} = \frac{vd}{L} \sqrt{\frac{\rho_g}{\xi_n L}},$$

$$I_{\text{mac}} \sim v/\sqrt{\xi_n L/\rho_g} = v \sqrt{\frac{\rho_g}{\xi_n L}}.$$

From the above equations, we observe that the characteristic value of I_{mac} reduces to a multiple of the *Froude number* (Fr) in gravity loaded systems. To this end, Sunday et al. (45) explored the existence of macro-inertial effects during high-speed granular intrusions and observed insignificant contributions of macro-inertial effects in the material force response for $Fr < 1.5$, which gives $I_{\text{mac}} \lesssim 0.48$. Similarly, Agarwal et al. (25), observed insignificant macro-inertial effects (macro-inertial forces $< 10\%$ of static resistive forces i.e. $\rho A v^2/K|z| < 10\%$) in granular plate intrusions at $I_{\text{mac}} < 0.16$. Thus, we impose an upper limit of 0.15 on I_{mac} to be quasi-static. The amount I affects the flow can be quantified by how much it changes the apparent internal friction (46, 47). To keep these changes bounded by 10% we set an upper bound on the characteristic value of I to be 0.010 so as to ensure quasi-static conditions. For all the test cases used in this study, we choose system parameters in such a way that I and I_{mac} are always below above mentioned limits keeping their motions in quasi-static limits. The test cases 1-10 are continuum simulation

that use a rate-independent constitutive law and have $I_{\text{mac}} \sim 0.02$ ($L \approx 0.07\text{m}$, $v = 0.1\text{m/s}$, $\xi_n = 0.92 \times 10^6$, $\rho_c = 3000\text{kg/m}^3$). In the DEM based cylinder drill test cases, we find $I < 0.002$ and $I_{\text{mac}} < 0.07$ ($L \approx 0.10\text{m}$, $\omega < \pi\text{rad/s}$, $v_{\text{intruder}} = 0.1\text{m/s}$, $\xi_n = 0.12 \times 10^6$, $\rho_g = 2470\text{kg/m}^3$). Similarly, in the bunny drill test case, we find $I \approx 0.004$ and $I_{\text{mac}} \sim 0.13$ ($L \approx 0.10\text{m}$, $\omega = 2\pi\text{rad/s}$, $v_{\text{intruder}} = 0.1\text{m/s}$, $\xi_n = 0.12 \times 10^6$, $\rho_g = 2470\text{kg/m}^3$). Thus, 3D-RFT is a valid approach for modeling all the test cases considered in this study, based on the insignificance of micro- and macro- inertial force contributions.

Continuum approach accuracy validation. Several studies in the past have verified the accuracy of this constitutive formulation in plane-strain problems. We use the 3D numerical implementation of MPM developed by Baumgarten and Kamrin (29) for this study which has been successfully used for modeling complex problems in the past (29, 30). For the continuum model to be useful to determine input data for a 3D-RFT, it must be shown to reliably match experiments for 3D plate intrusions. We test this in two scenarios.

In the first test case, we check if the 3D-continuum simulations can regenerate the experimental variation of force/depth/area on flat plates in submerged granular beds from Li et al.(14). This experimental data was also used by Li et al.(14) in the generation of 2D-RFT form. We use an effective materials density of $\rho_c = 1450\text{kg/m}^3$ (loose glass beads, $\rho_g = 2500\text{kg/m}^3$, $\phi_c = 0.58$) inline with Li et al.(14) experiments and an approximate internal friction value for glass beads as $\mu_{\text{int}} = 0.4$. The media-plate surface friction was taken as $\mu_{\text{surf}} = 0.4$. The relative values of the forces from continuum results remarkably match the experimental observations. The absolute values from continuum results, however, are higher than experiments by a constant multiplicative factor of ~ 1.1 . A smaller value of μ_{int} for glass beads could have provided a closer match to the experiments as the graphs are not expected to change

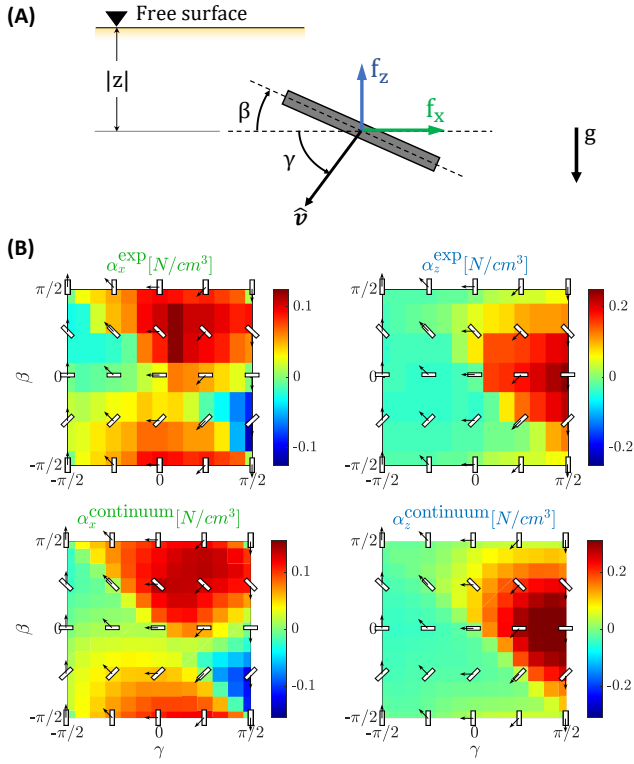


Fig. 9. Experiment vs Continuum Model — Comparison of in-plane plate motions: (A) Schematic of plate orientation angle β and γ for in-plane motion study conducted using 3D simulation setup shown in figure 4. (B) Force/area/depth (α) from Li et al. (14) experiments (top) and continuum simulations (bottom). The plate configurations are also overlaid on graphs for clarity. The plates had no twist ($\psi = 0$) in regards to 3D-RFT definitions in these tests. Both the experiments and the simulations use glass beads with grain density (ρ_g) of 2500 kg/m^3 and a packing fraction (ϕ_c) of 0.58. Internal friction is $\mu_{\text{int}} = 0.4$ and surface friction, $\mu_{\text{surf}} = 0.4$ for continuum simulations to match reported values in Li et al. (14).

their shape with changing internal friction values (14). But we do not attempt the exact calibration as the purpose of the test was to verify the accuracy of the continuum formulation and implementation. These results establish sufficient efficacy of the continuum model for plate motions in which the velocity, plate normal, and gravity or co-planar.

In the second test case, we assess the quantitative accuracy of the continuum approach in modeling in-plane as well as out-of-plane forces. We consider a study Maladen et al. (48) which measured the normal and tangential forces on submerged plates moving horizontally in granular media as a function of plate twist (see Fig 10 (top) for angles definition). The material properties are provided in the figure caption. The continuum results match observations from Maladen et al. (48) well.

The combination of the above two studies establishes the overall accuracy of the continuum model and its implementation for both in-plane and out-of-plane inputs and outputs in plate intrusion problems.

3D-RFT reference data generation. We use a large combination of material properties ($\rho_c, \mu_{\text{int}}, \mu_{\text{surf}}$) and 3D-RFT reference variables (β, γ, ψ) to generate continuum modeling-based reference data for evaluating the 3D-RFT form. In regards to the material properties we use five material internal friction values ($\mu_{\text{int}} = [0.3, 0.4, 0.5, 0.7, 0.9]$) with two values of surface friction (μ_{surf}) in each case. For $\mu_{\text{int}} = 0.4$ we use 3 instead of 2 μ_{surf} values. For each of the 11 combinations of μ_{int} and μ_{surf} , we conduct plate intrusions at 7 combinations of plate tilt angle ($\beta = -\pi/2 : \pi/6 : \pi/2$ rad), 7 combinations of velocity direction angle ($\gamma = -\pi/2 : \pi/6 : \pi/2$ rad), and 4 combinations of plate twist angle ($\psi = 0 : \pi/6 : \pi/2$ rad). For the $\{\mu_{\text{int}} = 0.40, \mu_{\text{surf}} = 0.15\}$, we use 13 combinations

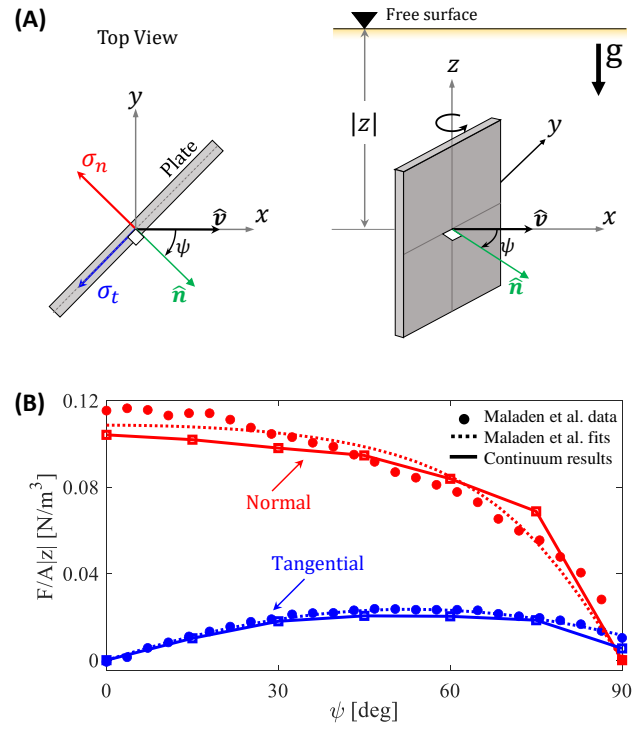


Fig. 10. Experiment vs Continuum Model: Dependence on twist angle: (A) Schematic of plate orientations, and (B) variations of normal (red) and tangential (blue) forces from Maladen et al. (48) experiments (\bullet marker), their analytical fits to their results (dotted lines), and continuum simulations (\blacksquare marker with solid line). The forces are normalized by the plate center-depth ($|z|$) and plate area. Experiments (loosely packed 3 mm glass particles) as well as simulation use glass beads ($\rho_g = 2500 \text{ kg/m}^3$ and $\rho_c = 0.6$) as the granular media. Continuum simulations use $\mu_{\text{int}} = 0.4$ and $\mu_{\text{surf}} = 0.27$ in accordance with reported experimental values. The original Maladen et al. (48) results used a twist angle ($\beta_d = \pi/2 - \psi$) as the x -axis in their plots. We have modified the plots to have $\psi = \pi/2 - \beta_d$ on x -axis for simplifying the discussion.

of β ($\pi/2 : \pi/6 : \pi/2$ rad), 13 combinations of γ ($-\pi/2 : \pi/6 : \pi/2$ rad), and 4 combinations of ψ ($0 : \pi/6 : \pi/2$ rad). Additionally, we conduct plate intrusion simulations at $\{\mu_{\text{int}} = 0.2, \mu_{\text{surf}} = 0.2\}$ and $\{\mu_{\text{int}} = 0.1, \mu_{\text{surf}} = 0.1\}$ at $\psi = 0$ rad to evaluate ξ_n at $\mu_{\text{int}} = 0.1$ and 0.2. We do not explore ψ in $[-\pi/2 : 0]$ rad range for the reference data as α_r, α_z , and α_θ are known to be even, even, and odd (resp.) in ψ from ‘plate twist symmetry’. The polynomial fits for f_1, f_2 , and f_3 are provided in the Supplementary Information (Table S3 and table S4).

3D-RFT Implementation. We use an explicit iterative scheme to implement 3D-RFT in this study. The strategy primarily consists three parts — (1) discretizing the intruder surface into small sub-surfaces, (2) finding the sub-surface forces using sub-surface orientation angles (β and ψ), velocity angle (γ), area (ds), and depth from the free surface ($|z|$), and (3) summing over all sub-surfaces to find the net resistive force and moment response. A step-by-step implementation of the strategy is provided below:

Step 1: Discretize the intruder surface into small plane sub-surface elements. We use the open-source software, ‘Blender’ (version 2.91) for modeling and discretizing various intruder geometries in our study (using .wrl format).

Step 2: Calculate the velocity direction vector \hat{v} , surface normal \hat{n} , and depth from the free surface $|z|$ for each sub-surface. Repeat Steps 3-11 for each sub-surface.

Step 3: Check if $\hat{n} \cdot \hat{v} \geq 0$ (sub-surface is a ‘leading edge’) and $z < 0$ (sub-surface is submerged in the media). If both the

conditions are met, follow Steps 4-11. If they are not, set the sub-surface resistive force to zero and consider the next sub-surface.

Step 4: Find local coordinate frame $\{\hat{r}, \hat{\theta}, \hat{z}\}$ using eq 11.

Step 5: Find RFT characteristic angles $\{\beta, \gamma, \psi\}$ using \hat{v} , \hat{n} , and local coordinate frame $\{\hat{r}, \hat{\theta}, \hat{z}\}$ as follows:

Find the surface characteristic angle β as:

$$\begin{aligned} \beta = & \quad -\cos^{-1}(\hat{n} \cdot \hat{z}) & \text{if } \hat{n} \cdot \hat{r} \geq 0 \ \& \ \hat{n} \cdot \hat{z} \geq 0 \\ & +\pi - \cos^{-1}(\hat{n} \cdot \hat{z}) & \text{if } \hat{n} \cdot \hat{r} \geq 0 \ \& \ \hat{n} \cdot \hat{z} < 0 \\ & \cos^{-1}(\hat{n} \cdot \hat{z}) & \text{if } \hat{n} \cdot \hat{r} < 0 \ \& \ \hat{n} \cdot \hat{z} \geq 0 \\ & -\pi + \cos^{-1}(\hat{n} \cdot \hat{z}) & \text{if } \hat{n} \cdot \hat{r} < 0 \ \& \ \hat{n} \cdot \hat{z} < 0 \end{aligned} \quad [16]$$

Remember that this β corresponds to only 'leading edges' as non 'leading-edge' sub-surface never reach this step.

Find the velocity characteristic angle γ as:

$$\begin{aligned} \gamma = & \quad \cos^{-1}(\hat{v} \cdot \hat{r}) & \text{if } \hat{v} \cdot \hat{z} \leq 0 \\ & -\cos^{-1}(\hat{v} \cdot \hat{r}) & \text{if } \hat{v} \cdot \hat{z} \geq 0 \end{aligned} \quad [17]$$

Find the surface characteristic angle ψ as:

$$\begin{aligned} \psi = & \quad \tan^{-1}\left(\frac{(\hat{n}_{r\theta} \cdot \hat{r})}{(\hat{n}_{r\theta} \cdot \hat{r})}\right) \\ \text{where, } \hat{n}_{r\theta} = & \quad \frac{\hat{n} - (\hat{n} \cdot \hat{z})\hat{z}}{|\hat{n} - (\hat{n} \cdot \hat{z})\hat{z}|} \end{aligned} \quad [18]$$

If $|\hat{n} - (\hat{n} \cdot \hat{z})\hat{z}| = 0$, set $\psi = 0$. In case both \hat{v} and \hat{n} align to \hat{z} ($\gamma = \pm\pi/2$ and $\psi = 0$), set \hat{r} in global x -direction.

Step 6: Calculate $\{x_1, x_2, x_3\}$ using Eq 15 and calculate f_1, f_2, f_3 using table S3 (or table S4).

Step 7: Calculate the values of $\{\alpha_r^{\text{gen}}, \alpha_\theta^{\text{gen}}, \alpha_z^{\text{gen}}\}$ using Eq 14 and table S3.

Step 8: Estimate the media specific scaling factor ξ_n using expected functional form of ξ_n from section S1 and Fig S3 of the Supplementary Information if the media effective density (ρ_c), gravity magnitude (g), and media internal friction coefficient (μ_{int}) are known. Alternatively, obtain ξ_n from vertical plate intrusion experiments (intrusion of a thin flat plate of area ds at $\beta = 0$, $\psi = 0$, and $\gamma = \pi/2$) using the following formula:

$$\xi_n = \frac{F_{\text{vertical}}}{\alpha_z^{\text{gen}}(\beta = 0, \gamma = \pi/2, \psi = 0) \times ds \times |z|} \quad [19]$$

where, $|z|$ corresponds to the average depth of the plate from the free surface at which the force is measured.

Step 9: Calculate the system specific α_n and α_t in the local coordinate frame using Eq 6-7 and add them up (Eq 5) to get α .

Step 10: Calculate $\{\alpha_x, \alpha_y, \alpha_z\}$ using Eq 13 by substituting triad $\{\hat{r}, \hat{\theta}, \hat{z}\}$ from Eq 11.

Step 11: Calculate the net resistive force on the sub-surface by multiplying the triad $\{\alpha_x, \alpha_y, \alpha_z\}$ with sub-surface depth ($|z_i|$), and area (ds_i)

Step 12: Sum over all the sub-surfaces to find the net force and moment on the intruder.

Once the net resistive force on the intruder is known, one can use momentum balance equations to further model the intruder

motion. Convergence studies are also done to determine the discretization of the intruder shape.

ACKNOWLEDGMENTS. SA, and KK acknowledge support from Army Research Office (ARO) grants W911NF1510196 and W911NF1810118 and support from the U.S. Army Tank-Automotive Research, Development and Engineering Center (TARDEC). DG acknowledges support from ARO grant W911NF-18-1-0120. SA thanks Aaron Baumgarten, who provided the authors with his 3D-MPM model implementation. We also thank Andras Karsai for helpful discussions on potential forms of 3D-RFT.

1. Sigurdur T Thoroddsen and Amy Q Shen. Granular jets. *Physics of Fluids*, 13(1):4–6, 2001.
2. Shashank Agarwal, Carmine Senatore, Tingnan Zhang, Mark Kingsbury, Karl Iagnemma, Daniel I Goldman, and Ken Kamrin. Modeling of the interaction of rigid wheels with dry granular media. *Journal of Terramechanics*, 85:1–14, 2019.
3. Perrin E Schiebel, Henry C Astley, Jennifer M Rieser, Shashank Agarwal, Christian Hubicki, Alex M Hubbard, Keilmar Diaz, Joseph R Mendelson III, Ken Kamrin, and Daniel I Goldman. Mitigating memory effects during undulatory locomotion on hysteretic materials. *Elife*, 9:e51412, 2020.
4. Natalia Artemieva and Boris Ivanov. Launch of martian meteorites in oblique impacts. *Icarus*, 171(1):84–101, 2004.
5. Laura K Treers, Cyndia Cao, and Hannah S Stuart. Granular resistive force theory implementation for three-dimensional trajectories. *IEEE Robotics and Automation Letters*, 6(2):1887–1894, 2021.
6. Auke J Ijspeert. Biorobotics: Using robots to emulate and investigate agile locomotion. *science*, 346(6206):196–203, 2014.
7. Devaraj Van Der Meer. Impact on granular beds. *Annual review of fluid mechanics*, 49:463–484, 2017.
8. Rui He, Corina Sandu, Amir K Khan, A Glenn Guthrie, P Schalk Els, and Herman A Hamersma. Review of terramechanics models and their applicability to real-time applications. *Journal of Terramechanics*, 81:3–22, 2019.
9. Mieczyslaw Gregory Bekker. Introduction to terrain-vehicle systems. *University of Michigan Press*, 1969.
10. Jo-Yung Wong and AR Reece. Prediction of rigid wheel performance based on the analysis of soil-wheel stresses part i. performance of driven rigid wheels. *Journal of Terramechanics*, 4(1):81–98, 1967.
11. Hans B Pacejka and Egbert Bakker. The magic formula tyre model. *Vehicle system dynamics*, 21(S1):1–18, 1992.
12. James Gray and GJ Hancock. The propulsion of sea-urchin spermatozoa. *Journal of Experimental Biology*, 32(4):802–814, 1955.
13. Charles J Brokaw. Flagellar propulsion. *Journal of Experimental Biology*, 209(6):985–986, 2006.
14. Chen Li, Tingnan Zhang, and Daniel I Goldman. A terradynamics of legged locomotion on granular media. *science*, 339(6126):1408–1412, 2013.
15. Lei Huang, Junda Zhu, Yufeng Yuan, and Yh Yin. A dynamic resistive force model for designing mobile robot in granular media. *IEEE Robotics and Automation Letters*, 2022.
16. Ryan D Maladen, Yang Ding, Chen Li, and Daniel I Goldman. Undulatory swimming in sand: subsurface locomotion of the sandfish lizard. *science*, 325(5938):314–318, 2009.
17. Tingnan Zhang and Daniel I Goldman. The effectiveness of resistive force theory in granular locomotion. *Physics of Fluids*, 26(10):101308, 2014.
18. Pierre Jop, Yoël Forterre, and Olivier Pouliquen. A constitutive law for dense granular flows. *Nature*, 441(7094):727, 2006.
19. GDR MiDi. On dense granular flows. *The European Physical Journal E*, 14(4):341–365, 2004.
20. Nick Gravish, Paul B. Umbanhowar, and Daniel I. Goldman. Force and flow at the onset of drag in plowed granular media. *Physical Review E*, 89(4), apr 2014.
21. Hesam Askari and Ken Kamrin. Intrusion rheology in grains and other flowable materials. *Nature materials*, 15(12):1274, 2016.
22. Sachith Dunatunga and Ken Kamrin. Continuum modelling and simulation of granular flows through their many phases. *Journal of Fluid Mechanics*, 779:483–513, 2015.
23. Sachith Dunatunga and Ken Kamrin. Continuum modeling of projectile impact and penetration in dry granular media. *Journal of the Mechanics and Physics of Solids*, 100:45–60, 2017.
24. Shashank Agarwal, Andras Karsai, Daniel I Goldman, and Ken Kamrin. Efficacy of simple continuum models for diverse granular intrusions. *Soft Matter*, 17(30):7196–7209, 2021.
25. Shashank Agarwal, Andras Karsai, Daniel I Goldman, and Ken Kamrin. Surprising simplicity in the modeling of dynamic granular intrusion. *Science Advances*, 7(17):eabe0631, 2021.
26. Shashank Agarwal et al. Development of a reduced-order modeling technique for granular locomotion. Master's thesis, Massachusetts Institute of Technology, 2019.
27. James Slonaker, D Carrington Motley, Qiong Zhang, Stephen Townsend, Carmine Senatore, Karl Iagnemma, and Ken Kamrin. General scaling relations for locomotion in granular media. *Physical Review E*, 95(5):052901, 2017.
28. Qiong Zhang, Stephen Townsend, and Ken Kamrin. Expanded scaling relations for locomotion in sloped or cohesive granular beds. *Physical Review Fluids*, 5(11):114301, 2020.
29. Aaron S Baumgarten and Ken Kamrin. A general fluid–sediment mixture model and constitutive theory validated in many flow regimes. *Journal of Fluid Mechanics*, 861:721–764, 2019.
30. Aaron S Baumgarten and Ken Kamrin. A general constitutive model for dense, fine-particle suspensions validated in many geometries. *Proceedings of the National Academy of Sciences*, 116(42):20828–20836, 2019.
31. François Guillard, Yoël Forterre, and Olivier Pouliquen. Lift forces in granular media. *Physics of Fluids*, 26(4):043301, 2014.

32. Wenting Kang, Yajie Feng, Caishan Liu, and Raphael Blumenfeld. Archimedes' law explains penetration of solids into granular media. *Nature communications*, 9(1):1–9, 2018.
33. GF Smith. On isotropic functions of symmetric tensors, skew-symmetric tensors and vectors. *International journal of engineering science*, 9(10):899–916, 1971.
34. Greg Turk and Marc Levoy. Zippered polygon meshes from range images. In *Proceedings of the 21st annual conference on Computer graphics and interactive techniques*, pages 311–318, 1994.
35. Hirotaka Suzuki, Kota Katsushima, and Shingo Ozaki. Study on applicability of rft to traveling analysis of wheel with grousers: Comparison with dem analysis as a virtual test. *Journal of Terramechanics*, 83:15–24, 2019.
36. Swapnil Pravin, Brian Chang, Endao Han, Lionel London, Daniel I Goldman, Heinrich M Jaeger, and S Tonia Hsieh. Effect of two parallel intruders on total work during granular penetrations. *Physical Review E*, 104(2):024902, 2021.
37. Nick Gravish, Paul B Umbanhowar, and Daniel I Goldman. Force and flow transition in plowed granular media. *Physical review letters*, 105(12):128301, 2010.
38. Hiroaki Katsuragi and Douglas J Durian. Unified force law for granular impact cratering. *Nature Physics*, 3(6):420, 2007.
39. Alex A Francoeur and Kelly M Dorgan. Burrowing behavior in mud and sand of morphologically divergent polychaete species (annelida: Orbiniidae). *The Biological Bulletin*, 226(2): 131–145, 2014.
40. Shivakumar Athani and Pierre Rognon. Pulling objects out of cohesive granular materials. *Granular Matter*, 23(3):1–10, 2021.
41. Antoine Humeau, Miguel Piñeirua, Jérôme Crassous, and Jérôme Casas. Locomotion of ants walking up slippery slopes of granular materials. *Integrative Organismal Biology*, 1(1): obz020, 2019.
42. AS Soliman, SR Reid, and W Johnson. The effect of spherical projectile speed in ricochet off water and sand. *International Journal of Mechanical Sciences*, 18(6):279–in2, 1976.
43. Esteban Wright, Alice C Quillen, Juliana South, Randal C Nelson, Paul Sánchez, John Siu, Hesam Askari, Miki Nakajima, and Stephen R Schwartz. Ricochets on asteroids: Experimental study of low velocity grazing impacts into granular media. *Icarus*, 351:113963, 2020.
44. Henry C Astley, Joseph R Mendelson III, Jin Dai, Chaohui Gong, Baxi Chong, Jennifer M Rieser, Perrin E Schiebel, Sarah S Sharpe, Ross L Hatton, Howie Choset, et al. Surprising simplicities and syntheses in limbless self-propulsion in sand. *Journal of Experimental Biology*, 223(5):jeb103564, 2020.
45. Cecily Sunday, Naomi Murdoch, Arnaud Wilhelm, Melanie Drilleau, Yun Zhang, Simon Tardivel, and Patrick Michel. The influence of gravity on granular impacts-ii. a gravity-scaled collision model for slow interactions. *Astronomy & Astrophysics*, 658:A118, 2022.
46. GDR MiDi gdrmidi@polytech.univ-mrs.fr <http://www.lmgc.univ-montp2.fr/MIDI/>. On dense granular flows. *The European Physical Journal E*, 14:341–365, 2004.
47. Frédéric Da Cruz, Sacha Emam, Michaël Prochnow, Jean-Noël Roux, and François Chevoir. Rheophysics of dense granular materials: Discrete simulation of plane shear flows. *Physical Review E*, 72(2):021309, 2005.
48. Ryan D Maladen, Yang Ding, Paul B Umbanhowar, Adam Kamor, and Daniel I Goldman. Mechanical models of sandfish locomotion reveal principles of high performance subsurface sand-swimming. *Journal of The Royal Society Interface*, 8(62):1332–1345, 2011.

DRAFT